Evolution of Severe and Nonsevere Convection Inferred from GOES-Derived Cloud Properties

JOHN L. CINTINEO

Cooperative Institute of Meteorological Satellite Studies, University of Wisconsin—Madison, Madison, Wisconsin

MICHAEL J. PAVOLONIS

Advanced Satellite Products Team, NOAA/NESDIS/Center for Satellite Applications and Research, Madison, Wisconsin

JUSTIN M. SIEGLAFF

Cooperative Institute of Meteorological Satellite Studies, University of Wisconsin—Madison, Madison, Wisconsin

ANDREW K. HEIDINGER

Advanced Satellite Products Team, NOAA/NESDIS/Center for Satellite Applications and Research, Madison, Wisconsin

(Manuscript received 3 December 2012, in final form 24 April 2013)

ABSTRACT

Geostationary satellites [e.g., the Geostationary Operational Environmental Satellite (GOES)] provide high temporal resolution of cloud development and motion, which is essential to the study of many mesoscale phenomena, including thunderstorms. Initial research on thunderstorm growth with geostationary imagery focused on the mature stages of storm evolution, whereas more recent research on satellite-observed storm growth has concentrated on convective initiation, often defined arbitrarily as the presence of a given radar echo threshold. This paper seeks to link the temporal trends in robust GOES-derived cloud properties with the future occurrence of severe-weather radar signatures during the development phase of thunderstorm evolution, which includes convective initiation. Two classes of storms (severe and nonsevere) are identified and tracked over time in satellite imagery, providing distributions of satellite growth rates for each class. The relationship between the temporal trends in satellite-derived cloud properties and Next Generation Weather Radar (NEXRAD)-derived storm attributes is used to show that this satellite-based approach can potentially be used to extend severe-weather-warning lead times (with respect to radar-derived signatures), without a substantial increase in false alarms. In addition, the effect of varying temporal sampling is investigated on several storms during a period of GOES super-rapid-scan operations (SRSOR). It is found that, from a satellite perspective, storms evolve significantly on time scales shorter than the current GOES operational scan strategies.

1. Background

First launched in the late 1960s and 1970s, geostationary weather satellites [e.g., Applications Technology Satellite (Suomi and Parent 1968), Synchronous Meteorological Satellites (e.g., Legeckis 1975), and Geostationary Operational Environmental Satellite (GOES; Menzel and Purdom 1994)] provide frequent observations of clouds and weather systems. Convective clouds are a subset of clouds that develop on short time scales (from minutes to hours), and frequent observation is necessary to understand the physical processes related to convective clouds as well as to forecast the development/growth of such clouds. Purdom (1993) provides an overview of the role of satellite observations from convective clouds (to be specific, tornadic thunderstorms), including atmospheric temperature and moisture retrievals prior to initiation, forcing mechanisms during initiation, and satellite-inferred severity of mature thunderstorms.

In more specific terms, Adler and Fenn (1979a,b), Adler et al. (1985), and Reynolds (1980) were some of

Corresponding author address: John L. Cintineo, Cooperative Institute of Meteorological Satellite Studies, 1225 W. Dayton St., Madison, WI 53706.
E-mail: jlc248@gmail.com

DOI: 10.1175/JAMC-D-12-0330.1

the first to quantitatively use temporal trends of GOES infrared (IR) brightness temperature (BT) to determine the intensity of thunderstorms. These studies focused on distinguishing severe thunderstorms from nonsevere thunderstorms. Adler and Fenn (1979a,b) used all severe reports for verification, whereas Reynolds (1980) used only reports of severe hail for verification since, as he argued, severe hail is most directly related to updraft intensity and is least dependent upon boundary layer processes. These studies focused on the growth rate of thunderstorms that already had glaciated cloud tops (as the infrared BTs were below the homogeneous freezing point) and continued to grow to the tropopause (and, in some cases, the lower stratosphere). These case studies concluded that satellite-based growth rates of thunderstorms (as determined by decreasing BTs and the presence of very low BTs) could successfully be used to distinguish severe thunderstorms from nonsevere thunderstorms. These techniques required very low BTs and, in some cases, BTs that are consistent with the main storm updraft overshooting the tropopause, however. Given the level of maturity of thunderstorms for these techniques to be successful and given the high spatial and temporal resolutions of the current network of Next Generation Weather Radar (NEXRAD; Crum and Alberty 1993) over the continental United States (CONUS), these techniques provide limited added value over the CONUS (or anywhere else with good radar coverage).

Roberts and Rutledge (2003) more recently determined that the temporal trends of infrared BT from GOES could provide lead times of up to 30 min for storm initiation (production of 35-dBZ radar reflectivity). Building upon these studies, others have developed convective initiation/cloud-top-cooling methods to diagnose/nowcast thunderstorm initiation and intensification (Mueller et al. 2003; Mecikalski and Bedka 2006; Vila et al. 2008; Zinner et al. 2008; Sieglaff et al. 2011). Mecikalski et al. (2011) investigated the temporal trends of retrieved microphysical properties of growing convective clouds, relating them to physical properties of storm evolution prior to convective initiation. The focus of these studies was primarily on convective initiation and/or existing storm intensification and not on distinguishing between severe and nonsevere thunderstorms during the initial growth stages.

With the deployment of the CONUS-wide NEXRAD network in the early 1990s, radar-based storm observation and warning processes were revolutionized (Polger et al. 1994). Polger et al. (1994) showed that critical success index scores for severe-thunderstorm- and tornado-warning issuance nearly doubled relative to the pre-NEXRAD era. The lead time of severe-thunderstorm/tornado warnings averaged 14.9–17.3 min ahead of ground-truth observations, and tornado-warning lead time increased from 4.4 min prior to NEXRAD implementation to 8.8 min after NEXRAD implementation. Without question, NEXRAD observations are the critical tool for issuing severe-thunderstorm and tornado warnings.

The previously discussed satellite-based convective-initiation research indicates that robust satellite growth signatures exist prior to severe-weather signatures in NEXRAD observations. The goals of this paper are to examine whether the temporal evolution of satellite-based growth metrics from developing convective clouds can be used to distinguish severe from nonsevere thunderstorms and to demonstrate that these satellite-based growth signatures often occur prior to the appearance of robust severe-weather signatures in NEXRAD, leading to the possibility of increasing severe-thunderstorm-warning lead times even further. This investigation should provide a solid basis for the utility of satellite-observed growth rates upon entering an era of improved geostationary spatiotemporal resolution (~2 km in the IR; ~5 min over CONUS), beginning with the upcoming launch of GOES-R (Schmit et al. 2005). The organization of the remaining sections in this paper is as follows: section 2 contains data and methods, section 3 presents the analysis, and section 4 gives conclusions and future work.

2. Data and methods

a. Satellite data and algorithms

GOES-12 and *GOES-13* imager data are used in this study 1) as input into a cloud-object identification and tracking system and 2) as input into satellite algorithms that compute a cloud mask (Heidinger 2010), cloud-top phase (Pavolonis 2010a,b; Sieglaff et al. 2011), 11-μm top-of-troposphere cloud emissivity (Pavolonis 2010a), and cloud optical depth τ/effective radius r_e (Walther and Heidinger 2012). The output from these GOES algorithms is combined with the cloud-object-tracking output to calculate satellite-based convective-cloud-property evolution metrics.

The 11-μm top-of-troposphere cloud emissivity ε_{tot} is the 11-μm emissivity that a cloud would have if the radiative center of the cloud were located at the lower bound of the tropopause. For clouds with a large infrared optical depth, like the cumulus clouds analyzed in this study, ε_{tot} is a measure of how close the cloud radiative center is to the tropopause. A value of 1.0 is indicative of a cloud that is opaque in the IR and has an effective temperature consistent with the start of the tropopause. In general, ε_{tot} is only greater than 0.0 if a cloud is actually present. See Pavolonis (2010a) for a complete physical description of ε_{tot}. In spatial terms,

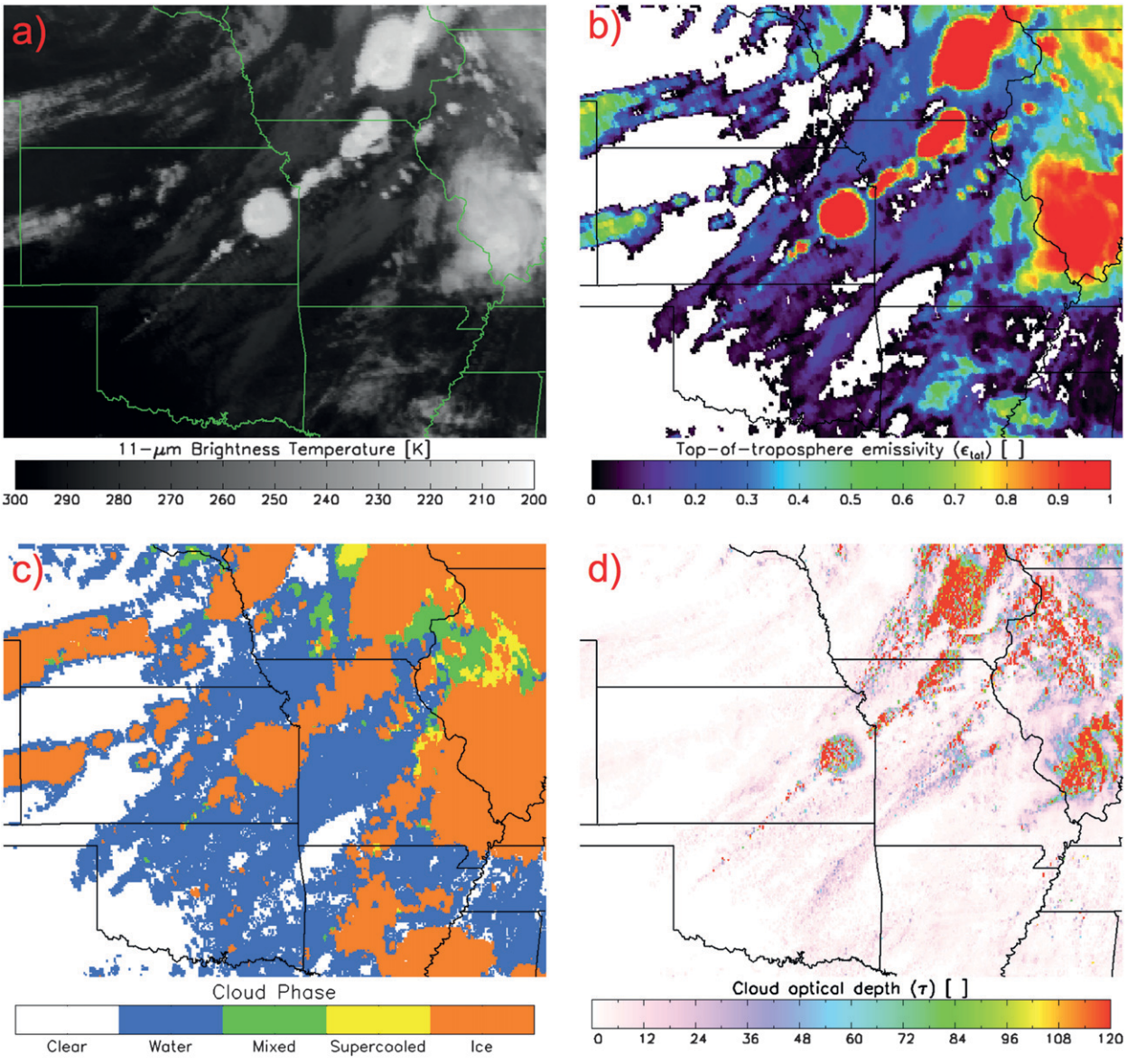

FIG. 1. A cold front over the central plains from 2215 UTC 13 May 2009, showing four satellite-derived fields used in the analysis: (a) 11-μm BT, (b) top-of-troposphere emissivity, (c) cloud phase, and (d) cloud optical depth.

ε_{tot} maintains the gradients observed in the 11-μm BT field (see Figs. 1a,b). Unlike BT, however, the ε_{tot} field is less sensitive to the thermodynamic state of the background, cloud-free, atmosphere. For example, a mature convective cloud nearing the tropopause will always have ε_{tot} values approaching 1.0, whereas the BT of such a cloud can vary on the order of tens of degrees Celsius both latitudinally and by season. In addition, ε_{tot} was determined to be more skillful in quantifying the vertical cloud growth of convective clouds than is IR BT (not shown) and therefore was chosen over the IR BT; ε_{tot} is also used for quantifying the horizontal expansion of developing convective clouds.

In addition, ε_{tot} is used as input into the cloud-object tracking system (described briefly later in the text). There are two advantages of using ε_{tot} over the IR BT within the cloud-object tracking system: 1) the fact that it is generally only valid (>0.0) for cloudy pixels and, as a result, clear-sky pixels are automatically excluded from cloud objects and 2) the aforementioned limited sensitivity to the background (cloud free) thermodynamic state of the atmosphere.

The GOES cloud-top-phase algorithm uses multispectral GOES observations as well as output from a multispectral GOES cloud mask (Heidinger et al. 2010) to determine the phase of cloudy GOES pixels. The

cloud-phase classifications include warm liquid water, supercooled liquid water, mixed phase, and ice (see example in Fig. 1c). The GOES cloud-top-phase output is used for determining the rate at which a developing convective cloud glaciates in the uppermost part of the cloud.

The GOES τ and r_e are computed only during daylight hours because the algorithm relies on measurements of reflected sunlight at visible and near-infrared wavelengths (see example in Fig. 1d). The algorithm utilizes a bispectral approach (0.64–3.9-μm channel pair on GOES) within an optimal estimation framework (Walther and Heidinger 2012). The GOES τ product, which is a measure of the vertically integrated extinction at 0.65 μm, is used to help quantify the horizontal expansion of developing convective clouds. The r_e product (Hansen and Travis 1974) provides a measure of the size of the hydrometeors that are contributing most significantly to the measured 3.9-μm radiation. As such, it may be a useful proxy for updraft strength prior to cloud-top glaciation, as stronger updrafts may have a weaker rate of change in r_e because of the shorter time available for cloud droplets to grow by coalescence, as supported by Rosenfeld et al. (2008). In this paper, r_e is used only for liquid water retrievals, as identified by the cloud-top-phase algorithm.

b. Cloud-object identification and tracking

A cloud-object identification and tracking system developed by Sieglaff et al. (2013, hereinafter S13) is employed in this study to create cloud objects for automated computation of temporal trends of convective-cloud growth metrics. The full details of the cloud-object tracking system are outside the scope of this text. The main points are described below, and the reader is encouraged to consult S13 for complete details. The S13 framework uses ε_{tot} as input to create cloud objects. A cloud object is simply a collection of adjacent pixels around a local maximum (of ε_{tot} in this case) grouped into a single entity on the basis of the rules of the S13 framework. Each cloud object is assigned a unique identifier and is tracked through space and time in subsequent GOES observations while maintaining the unique identifier. The S13 framework allows for the history of a variety of parameters to be maintained through a cloud object's lifetime, from infancy (as few as three GOES IR pixels) into the mature phase (hundreds of GOES IR pixels).

To be specific, the cloud objects are used to determine the time rate of change of the maximum ε_{tot} (vertical growth), ice cloud fraction (glaciation rate), area of $\varepsilon_{\text{tot}} \geq 0.8$ (horizontal growth), area of cloud $\tau \geq 40$ (horizontal growth), and mean cloud effective particle radius (updraft vigor) for each cloud object. The temporal trends are computed for two classes: a severe-thunderstorm dataset and a nonsevere-thunderstorm dataset. The severe-thunderstorm dataset includes 120 cloud objects, which were manually identified storms with observable growth rates (not obscured by large cloud shields) from 21 days between 2008 and 2012 (see Fig. 2a for their spatiotemporal distribution). The requirement for being classified as a severe thunderstorm was a surface hail or tornado report from the National Oceanic and Atmospheric Administration (NOAA)/National Climatic Data Center *Storm Data* publication (2008–12). The surface-hail/tornado criteria were chosen because of the ambiguity of wind-damage reports in the Storm Prediction Center storm-data record (Trapp et al. 2006). Reynolds (1980) also presents the use of severe hail reports as a means to classify severe thunderstorms. The nonsevere dataset (containing 864 objects) is composed of nonsevere convective clouds for a variety of geographical and seasonal locations over the CONUS that exhibited convective activity but that did not have any severe-weather reports. Figure 2b shows the spatiotemporal distribution of the latitude–longitude constrained boxes where the nonsevere storms were contained. The value in the upper-right corner of each box represents the number of storms added to the nonsevere dataset for each location. Cloud objects in these regions were added to the nonsevere class if they demonstrated some vertical growth (rate of change in maximum $\varepsilon_{\text{tot}} > 0$) and achieved at least 35 dBZ at -10°C at some point in their lifetime. The latter criterion was selected on the basis of recent research about convective initiation (Kain et al. 2013).

3. Analysis

a. Analysis of satellite-based growth metrics

For the severe and nonsevere distributions of each metric, the rate of change at each image time for an object is computed by simple subtraction using the previous image time and is then normalized by minutes elapsed. For the three vertical-growth-related predictors (maximum ε_{tot}, ice cloud fraction, and mean r_e), the maximum rate of change (between successive image times) in a given object "lifetime" is determined for all objects in the severe and nonsevere datasets. For the horizontal-growth predictors (object area encompassed by certain τ and ε_{tot} contours), the rate of change between each successive image pair is determined for all objects in each (severe and nonsevere) sample dataset. By collecting temporal trends in this manner, we aim to capture the largest vertical growth between successive images and the continued horizontal growth that occurs after the observable vertical growth has ceased. For each

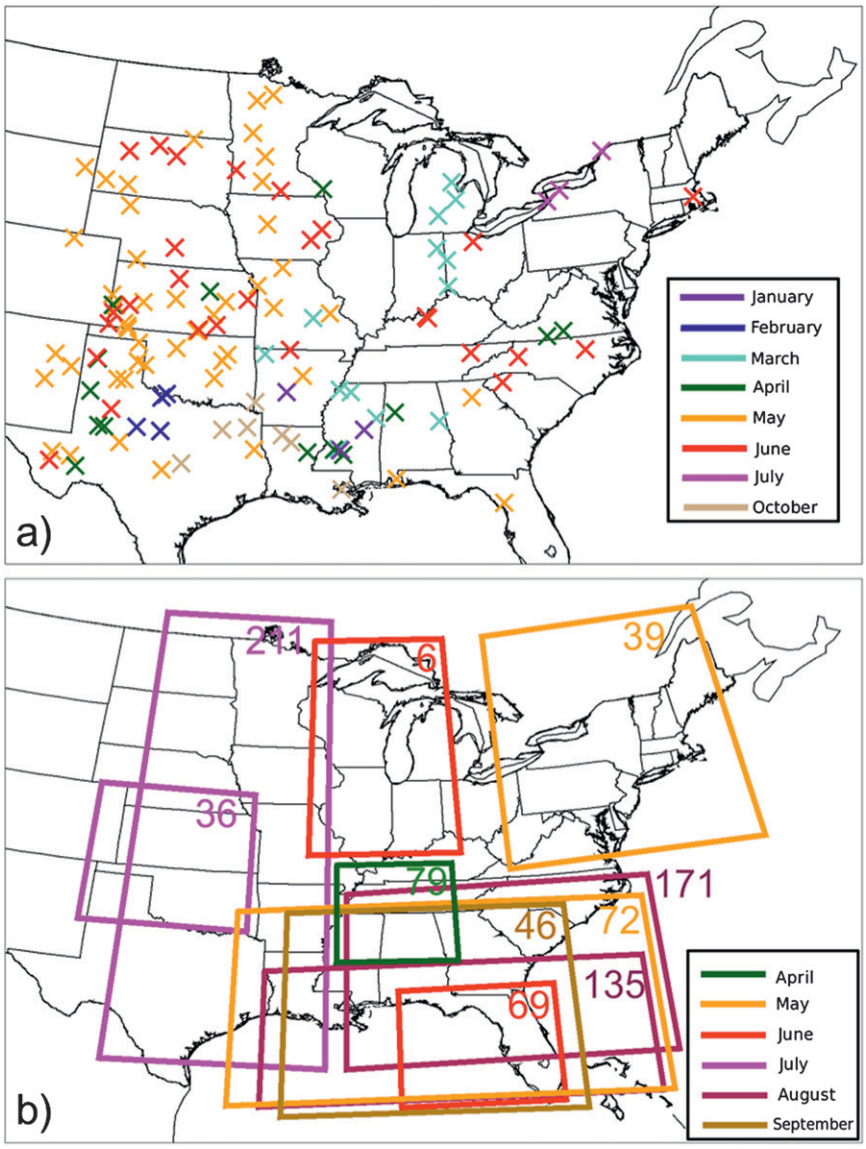

FIG. 2. (a) Each times sign marks the source point of a storm in the severe class, and the color shows the month in which the storm occurred. (b) Each box depicts the domain from where nonsevere storms were drawn, and the color shows the month in which the storms occurred. The values at the top right of each box are nonsevere-storm counts.

metric and class (severe and nonsevere), probability density functions were constructed and then smoothed using kernel density estimation (Wilks 2006) with standard normal kernels and variable bandwidths to approximate the true population probability density functions. Bandwidth selection was heuristic, attempting to preserve the underlying true distribution while eliminating variability produced by sparsely populated bins. The bandwidths are different for each predictor; they are identical for both the severe and nonsevere distributions of the given predictor, however. Table 1 gives bandwidth values, sample sizes, and the time at which the predictor is valid (which contributes to sample-size differences).

To test whether the means of the severe and nonsevere distributions of derived parameters are statistically different, a right-tailed (left tailed for r_e rate of change) Student's t test is performed (since the data samples are adequately large), with the null hypothesis being that the mean of the severe-storm distribution is not greater than the mean of the corresponding nonsevere-storm distribution for a given metric. Bootstrapping is also performed, in which each sample distribution is randomly resampled with replacement 5000

TABLE 1. Summary of statistical information for the satellite predictors, including bootstrapping results of 95% confidence intervals for sample mean and standard deviation for severe and nonsevere thunderstorms, as well as the *t*-test *p* value (comparing sample means) for each satellite growth predictor.

Predictor (unit)	Valid time	95% confidence interval: Mean	95% Confidence interval: Std dev	Bandwidth	Sample size	*t*-test *p* value
$\Delta\varepsilon_{\text{tot}}$ (min^{-1})						
Severe storms	Night and day	0.019 068–0.022 168	0.008 510–0.011 878	0.005	120	$O(10^{-44})$
Nonsevere storms	Night and day	0.007 763–0.008 714	0.007 884–0.009 065	0.005	864	$O(10^{-44})$
Δice (min^{-1})						
Severe storms	Night and day	0.0543–0.0657	0.0302–0.0382	0.018	97	$O(10^{-28})$
Nonsevere storms	Night and day	0.0210–0.0248	0.0266–0.0298	0.018	577	$O(10^{-28})$
$\Delta\varepsilon_{\text{tot–area}}$ ($\text{km}^2\,\text{min}^{-1}$)						
Severe storms	Night and day	47.8789–54.4834	37.7850–48.1438	11	485	$O(10^{-134})$
Nonsevere storms	Night and day	8.8487–11.2709	25.2904–36.3265	11	1911	$O(10^{-134})$
$\Delta\tau_{\text{area}}$ ($\text{km}^2\,\text{min}^{-1}$)						
Severe storms	Day only	22.8107–25.7401	31.9899–34.4272	8	1392	$O(10^{-93})$
Nonsevere storms	Day only	1.2343–1.6787	10.1006–10.6182	8	5861	$O(10^{-93})$
Δr_e ($\mu\text{m}\,\text{min}^{-1}$)						
Severe storms	Day only	0.1197–0.1942	0.1473–0.2403	0.25	76	0.0132
Nonsevere storms	Day only	0.0989–0.1241	0.1366–0.1823	0.25	446	0.0132

times to create confidence intervals of the mean and standard deviation of the distributions, approximating these population statistics empirically. Each of the new samples has the same size as the original sample (Wilks 2006). Table 1 summarizes the significance *p* values of the *t* tests, as well as the 95% confidence intervals for the means and standard deviations for the severe and nonsevere distributions for each predictor, computed empirically from the bootstrapped samples. The ensuing analysis demonstrates the degree of discrimination between the severe and nonsevere classes, irrespective of when a given rate of change occurred. The lead-time analysis in section 3b helps to determine when in the course of storm evolution these rates of change occur, measured with respect to weather-radar variables.

1) MAXIMUM ε_{TOT}

The rate of change in maximum ε_{tot}, denoted $\Delta\varepsilon_{\text{tot}}$, signals vertical growth in a cloud object. The hypothesis is that strong, more-persistent updrafts are more likely to create storms capable of severe hazards and should reach the upper troposphere/lower stratosphere sooner than weak updrafts do. Figure 3a shows the distributions of the lifetime maximum $\Delta\varepsilon_{\text{tot}}$ for the nonsevere and severe storms. The severe distribution demonstrates higher relative frequencies from about $0.012\,\text{min}^{-1}$ onward. Even at large rates of change, there is an order-of-magnitude difference between severe and nonsevere storms, although it is not explicitly visible. The mean $\Delta\varepsilon_{\text{tot}}$ of the severe storms is statistically greater than the mean $\Delta\varepsilon_{\text{tot}}$ of the nonsevere storms [significance *p* value = $O(10^{-44})$], signifying that the null hypothesis can most certainly be rejected. Given the difference in the shapes of the sample distributions and their large sample sizes, this result should not be surprising.

2) GLACIATION

The rate of glaciation is the rate of change in the fraction of the cloud object with a cloud-top phase of ice, denoted Δice. Our hypothesis is that faster vertical motion will cause a cloud top to convert from mostly water to mostly ice quicker than weaker vertical motion will. Figure 3b shows the sample distributions for Δice (min^{-1}) for severe and nonsevere storms. Objects that were initially mostly glaciated at the cloud top (ice cloud fraction greater than 0.5) were not included in these samples so as to capture only the conversion from mostly liquid water to mostly ice. Again, the maximum Δice for each object in the datasets is added to the distributions. The severe distribution is more heavily populated at higher values than is the nonsevere distribution, at Δice greater than approximately $0.03\,\text{min}^{-1}$. The *t* test again demonstrates that the mean growth for the severe distribution is statistically greater than that for the nonsevere distribution (see Table 1).

3) AREA OF $\tau \geq 40$

The rate of change in area of a cloud object measures the horizontal expansion of a storm once it loses positive buoyancy (at the cloud top) and cannot grow vertically any longer. The areal expansion of the storm is also a function of the depth of the storm's outflow, which is assumed to be primarily near the tropopause in this study. Faster-growing anvil clouds are again indicative of stronger, sustained updrafts and potentially severe-weather hazards. Mainly isolated storms

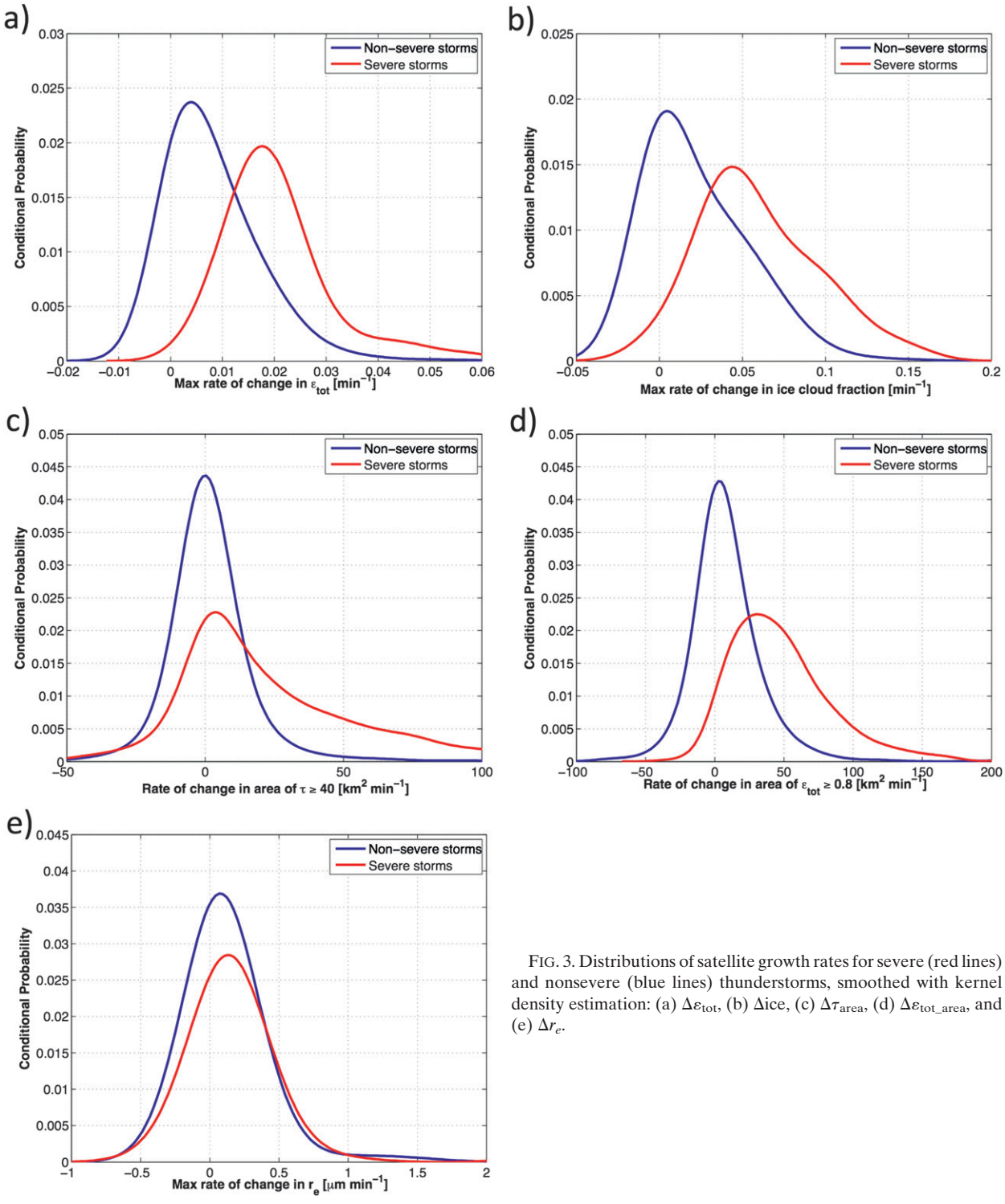

FIG. 3. Distributions of satellite growth rates for severe (red lines) and nonsevere (blue lines) thunderstorms, smoothed with kernel density estimation: (a) $\Delta\varepsilon_{tot}$, (b) Δice, (c) $\Delta\tau_{area}$, (d) $\Delta\varepsilon_{tot\_area}$, and (e) Δr_e.

were used, to avoid artificially large areal expansions as a result of multicell storms, which is a shortcoming of this predictor. The τ field identifies thicker cumuliform clouds in the midst of thin cirrus clouds but is only reliable when the solar zenith angle is less than 70°. Thus, only objects with a maximum solar zenith angle of less than 70° are included for this metric. Larger values of τ are representative of deeper cumulus

convection; the product noise is greater for larger τ (i.e., the signal is not as consistent from storm to storm), however. For example, one severe storm may exhibit many pixels of a high τ such as 100, and another severe storm may only have a few pixels of high τ. The threshold of $\tau \geq 40$ balances classification of cumuliform and cirrus, to noise tolerance. Furthermore, this threshold is similar to values of τ that were found in recent research to be characteristic of deep convective clouds (Young et al. 2012).

Figure 3c shows the severe and nonsevere sample distributions for the rate of change of area of $\tau \geq 40$ (denoted $\Delta\tau_{\text{area}}$; $\text{km}^2\,\text{min}^{-1}$). Recall that the distributions contain every area rate of change for an object, since we are concerned with sustained growth of a storm and not a single instance of strong horizontal growth (e.g., the storm's maximum growth rate). The severe distribution clearly has more weight at larger rates of change ($>10\,\text{km}^2\,\text{min}^{-1}$) than does the nonsevere distribution. This result suggests that nonsevere storms do not grow horizontally as quickly, or that their horizontal growth is not sustained. Again, the mean of the severe class is statistically greater than that of the nonsevere class (Table 1). The separation of these two distributions suggests that this metric may be skillful at discriminating between severe and nonsevere convection, especially for large rates of horizontal growth.

4) AREA OF $\varepsilon_{\text{TOT}} \geq 0.8$

Since the τ field is limited to when the maximum solar zenith angle is less than 70°, it is also beneficial to look at a diurnally invariant predictor to diagnose the horizontal growth/decay of storms. The 0.8 contour of ε_{tot} was chosen since we are interested in areal expansion at or near the tropopause. As described earlier, a value of 1.0 is indicative of an opaque cloud with a top at the bottom of the tropopause. A value of 0.8 ensures that anvil regions that are partially transparent to 11-μm radiation are included, as well as storms nearing the tropopause. The ε_{tot} contours between 0.75 and 0.85 yield similar results.

Similar to $\Delta\tau_{\text{area}}$, the rate of change in area of $\varepsilon_{\text{tot}} \geq 0.8$, denoted $\Delta\varepsilon_{\text{tot\_area}}$, demonstrates that severe storms exhibit stronger horizontal growth than do nonsevere storms (Fig. 3d). We see that the conditional probability for the severe storms exceeds its counterpart at about $20\,\text{km}^2\,\text{min}^{-1}$. The severe distribution is clearly much broader than the nonsevere distribution, and the two indeed come from different populations, as the mean $\Delta\varepsilon_{\text{tot\_area}}$ of the severe storms is statistically greater than that of the nonsevere storms (Table 1). This is consistent with a result of Soden (2004), who found that stronger convective events are associated with larger cirrus anvil shields. Thus, $\Delta\varepsilon_{\text{tot\_area}}$ may be a good alternative to $\Delta\tau_{\text{area}}$ for diagnosing severe-storm areal expansion when the solar zenith angle is too large or for enhancing the confidence that the storm is or will become severe.

5) MEAN EFFECTIVE RADIUS

The r_e, like τ, is only available when the solar zenith angle is less than 70°. The r_e property is derived close to cloud top, similar to the cloud phase. It is presumed that during the vertical growth stage of a thunderstorm the r_e in liquid water will increase, as collisions and coalescence occur more often as the larger hydrometeors are forced upward. For strong updrafts, however, the rate of increase in r_e may not be as large as the rate of increase for weak updrafts, as cloud droplets in weak updrafts have more time to grow by coalescence (Rosenfeld et al. 2008). Once the cloud begins to definitively glaciate in the uppermost part of the cloud, the interpretation of r_e is likely to change (e.g., Lindsey and Grasso 2008). Thus, in this analysis, r_e is only used if the cloud-top phase indicated liquid water. The maximum rate of change of the mean liquid water effective radius Δr_e for each storm was added to the final distributions. Figure 3e shows the sample distributions of Δr_e ($\mu\text{m min}^{-1}$) for severe and nonsevere storms. While still statistically significant, the practical significance of Δr_e in discerning updraft strength among severe and nonsevere thunderstorms is much smaller than the other predictors, as there is little apparent separation in the distributions of the two classes (Fig. 3e).

b. Lead-time analysis ahead of NEXRAD severe signatures

Several of these satellite predictors exhibit excellent discrimination between severe and nonsevere thunderstorms. While this is promising, it is also important to demonstrate the potential lead time that trends in satellite metrics of growing convection have, prior to significant NEXRAD features, as radar is by far the most widely used tool in forecasting severe-storm development. The University of Oklahoma/National Severe Storms Laboratory in Norman, Oklahoma, has provided merged, quality-controlled, CONUS-wide radar products (Lakshmanan et al. 2006, 2007a,b) to evaluate the lead-time potential of the satellite predictors.

The evaluation period contained a combined 29 days from January and March–October, spanning 2008–11. Of these days, 20 contained some storms from the severe or nonsevere classes. All storms that reached designated radar thresholds were evaluated on these days, however. As no single radar variable or threshold is exclusively indicative of severe weather, lead times to multiple thresholds of three radar variables are investigated:

1) maximum reflectivity at −10°C (REF10), 2) maximum vertically integrated liquid (VIL), and 3) maximum expected size of hail (MESH). All three maxima are instantaneous (not lifetime maxima). These three variables were chosen since each one captures the vertical extent and intensity of storms to some degree. Radar thresholds are preferable to storm reports for two reasons: 1) storm reports in the United States have a myriad of artifacts and biases (Doswell et al. 2005; Witt et al. 1998b; Kelly et al. 1985; Morgan and Summers 1982) and 2) we are attempting to approximate the amount of lead time relative to warning issuance (and not reported time) while making an effort to remove potential warning biases that different National Weather Service offices may exhibit (e.g., Polger et al. 1994).

The five satellite predictors of interest in this paper are $\Delta\varepsilon_{\text{tot}}$, Δr_e, Δice, $\Delta\tau_{\text{area}}$, and $\Delta\varepsilon_{\text{tot\_area}}$. For brevity, only $\Delta\varepsilon_{\text{tot}}$ and $\Delta\varepsilon_{\text{tot\_area}}$ are shown, because they have the lowest p values for the vertical and horizontal growth predictors, respectively. For clarity, lead times to the radar values are only shown for given rates of change that exceed a certain threshold, consistent with a storm that is "severe." For $\Delta\varepsilon_{\text{tot}}$, $0.02\,\text{min}^{-1}$ is used; for $\Delta\varepsilon_{\text{tot\_area}}$, $40\,\text{km}^2\,\text{min}^{-1}$ is used. The first rate of change (between successive images) to exceed the threshold for each predictor is used to measure lead time for each storm. See Figs. 3a and 3d for a reference on where these thresholds lie in the severe- versus nonsevere-storm distributions. The decreasing cumulative distribution functions (CDFs) of lead times are shown for each radar threshold for each predictor in Fig. 4.

1) Reflectivity at −10°C

The storm's REF10 is grouped in increments of 5 dBZ, from 30 to 65 dBZ. Over the 29 days, 7759 independent storms (cloud objects) achieved REF10 ≥ 30 dBZ. In Fig. 4a, the CDFs of lead times are displayed for different REF10 thresholds, for $\Delta\varepsilon_{\text{tot}} \geq 0.02\,\text{min}^{-1}$. The shaded box to the right of the lead-time threshold and above the REF10 threshold shows the percentage of storms that exceed that lead-time value, for the given radar threshold. For instance, approximately 65% of storms have lead times greater than 15 min prior to the first occurrence of REF10 ≥ 55 dBZ. The CDFs show that a significant proportion of storms with positive lead times occur at 45 ≤ REF10 < 55 dBZ and that substantial lead times are evident at REF10 ≥ 55 dBZ. This vertical predictor demonstrates beneficial lead time to moderate to strong REF10. Figure 4b demonstrates lead-time CDFs for $\Delta\varepsilon_{\text{tot\_area}} \geq 40\,\text{km}^2\,\text{min}^{-1}$. The majority of storms have negative lead times, prior to REF10 = 55 dBZ. Above that threshold, 35% of the storms have more than 5 min of lead time. At REF10 ≥ 60 dBZ, 45% of storms have lead times greater than 15 min. This result demonstrates that large $\Delta\varepsilon_{\text{tot\_area}}$ offers little lead time on REF10 except at large values. This is not surprising, as anvil expansion generally lags rapid updraft growth, which is consistent with results from early research on satellite-observed storms (Adler and Fenn 1979a,b).

2) Vertically integrated liquid

VIL measures the column-integrated liquid water content in storms (Greene and Clark 1972) and has been used for severe-weather forecasting, as enhanced reflectivity returns from hailstones often contaminate the liquid water signal. VIL was binned in increments of $5\,\text{kg}\,\text{m}^{-2}$, from 15 to $60\,\text{kg}\,\text{m}^{-2}$. During the 29 days, 2523 storms achieved VIL ≥ $15\,\text{kg}\,\text{m}^{-2}$. Figure 4c displays the CDFs of lead time to different thresholds of VIL, for $\Delta\varepsilon_{\text{tot}} \geq 0.02\,\text{min}^{-1}$. Fifty percent of storms have a lead time of 15 min or greater prior to VIL ≥ $20\,\text{kg}\,\text{m}^{-2}$, for this rate-of-change threshold. For the storms reaching VIL ≥ $35\,\text{kg}\,\text{m}^{-2}$, 65% have over 35 min of lead time; for storms achieving VIL ≥ $50\,\text{kg}\,\text{m}^{-2}$, 95% have lead times of greater than 15 min. The $\Delta\varepsilon_{\text{tot}}$ clearly demonstrates useful lead time, even at low to moderate VIL values. For $\Delta\varepsilon_{\text{tot\_area}} \geq 40\,\text{km}^2\,\text{min}^{-1}$, the CDFs of lead time still exhibit large numbers of storms with positive lead time (Fig. 4d), albeit at moderate to stronger VIL values. Approximately 20% of storms reaching VIL ≥ $25\,\text{kg}\,\text{m}^{-2}$ have lead times of greater than 15 min, and 35% of storms reaching VIL ≥ $40\,\text{kg}\,\text{m}^{-2}$ have lead times of greater than 15 min. For VIL ≥ $50\,\text{kg}\,\text{m}^{-2}$, almost 60% of storms have lead times that exceed 15 min.

3) Maximum expected size of hail

MESH is empirically derived from the severe hail index (Witt et al. 1998a), which is a reflectivity-weighted vertical integration from the 0°C isotherm to the top of the storm, neglecting reflectivity values below 40 dBZ and attempting to capture the integrated ice content of the storm. MESH does not have a one-to-one correspondence with hail size (Wilson et al. 2009), but Cintineo et al. (2012) showed that it is a good discriminator for the severe-sized hail threshold [1-in. (25.4 mm) diameter]. Stronger MESH certainly indicates strong reflectivity high into the atmosphere. MESH was binned by 0.25 in., from 0.25 to 2.0 in. The 29 days in this lead-time analysis yielded 1534 storms with MESH ≥ 0.25 in. Figure 4e shows the lead-time CDFs for $\Delta\varepsilon_{\text{tot}} \geq 0.02\,\text{min}^{-1}$. Nearly 75% of storms have lead times that exceed 15 min, prior to MESH ≥ 0.5 in. Prior to MESH ≥ 1.0 in., the proportion increases to 85% with 15 min or greater of lead time. The CDFs of lead time for $\Delta\varepsilon_{\text{tot\_area}} \geq 40\,\text{km}^2\,\text{min}^{-1}$ demonstrate useful lead times

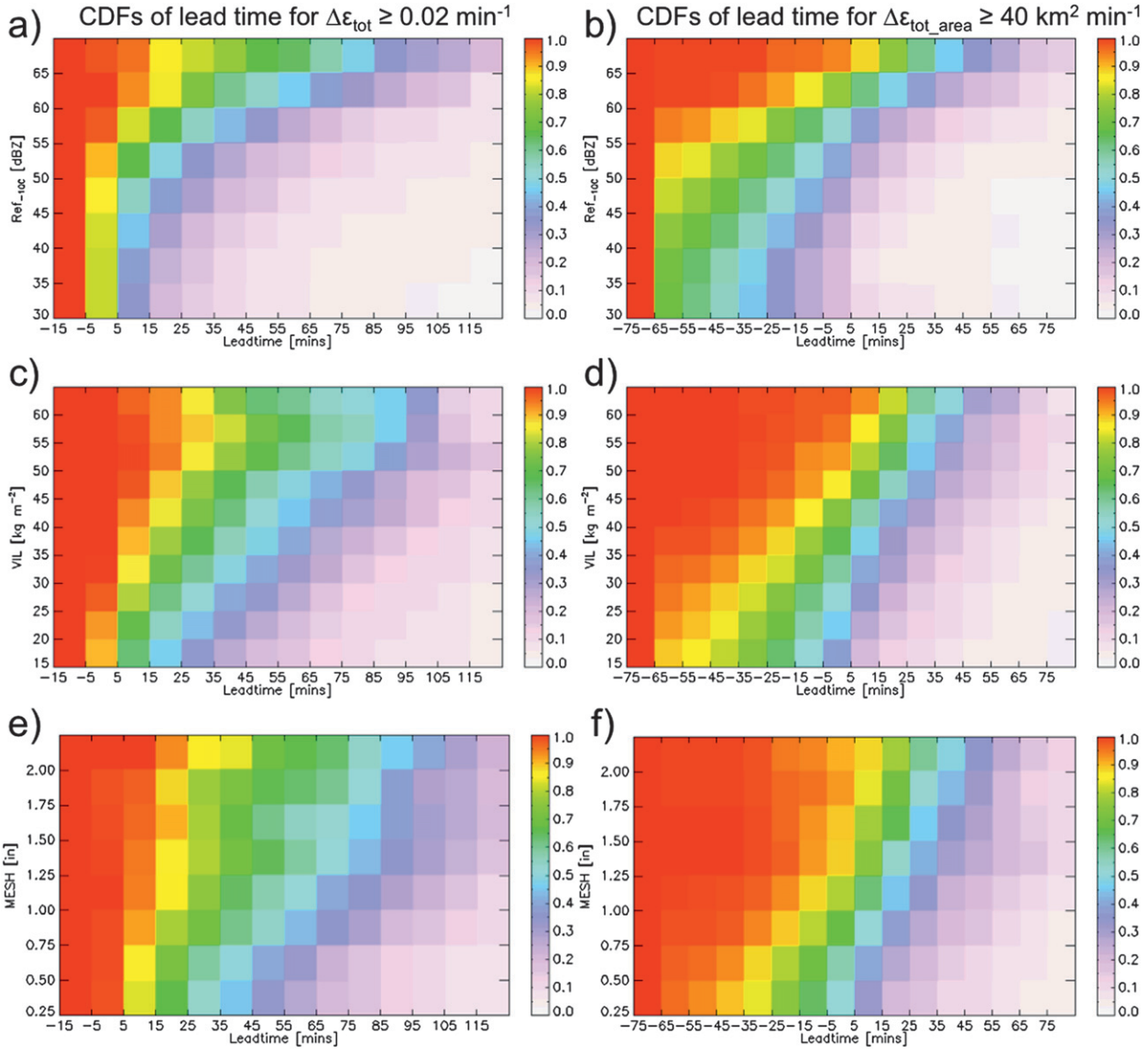

FIG. 4. Decreasing CDFs of lead time prior to radar-derived thresholds. Each row represents an independent CDF. Shown are $\Delta\varepsilon_{tot} \geq 0.02\,min^{-1}$ for (a) REF10, (c) VIL, and (e) MESH thresholds and $\Delta\varepsilon_{tot\_area} \geq 40\,km^2\,min^{-1}$ for (b) REF10, (d) VIL, and (f) MESH thresholds. See Figs. 3a and 3d for a reference of these satellite metric thresholds.

(Fig. 4f), although they are not as impressive as those for $\Delta\varepsilon_{tot}$. There are still 25% of storms with 15 min or more of lead time before 0.5-in. MESH is reached and 45% of storms with 15 min or more of lead time prior to 1.0 in. of MESH. Prior to very strong MESH (≥2.0 in.), approximately 75% of storms exhibit at least 15 min of lead time.

The $\Delta\varepsilon_{tot\_area}$ has good lead time for severe-level VIL and MESH, and $\Delta\varepsilon_{tot}$ has excellent lead time for VIL, MESH, and moderate REF10. Even though $\Delta\varepsilon_{tot\_area}$ and $\Delta\varepsilon_{tot}$ do not have substantial lead time for every storm, it is promising that large percentages of storms have modest to excellent lead times prior to severe radar signatures. It is clear, however, that satellite metrics that capture vertical growth should generally be more valuable for predicting which immature cumuliform clouds are most likely to produce severe weather later in their life cycles.

c. *The effect of temporal sampling on the observed growth rates of storms*

Numerous studies have estimated the vertical motion of continental and tropical deep convection using ground-based or airborne Doppler radar (e.g., Heymsfield and Schotz 1985; Heymsfield et al. 2010; Cecil et al. 2010). In an operational setting, convective cloud growth

can be inferred from high-temporal-resolution geostationary imagery. An opportunity presented itself when *GOES-14* was used, at times, in August and September of 2012 to conduct super-rapid-scan operations (SRSOR) for simulations of the next generation of GOES (GOES-R). Scenes of opportunity were identified each day, in which the satellite would scan a selected domain at 1-min frequency (with a 4-min scan gap every 30 min). This very high temporal resolution of growing thunderstorms provided an excellent occasion to see how varying temporal sampling of storms affected their observed growth rates. Storms that formed over Missouri and Arkansas on 16 August 2012 were investigated. These data were acquired from the University of Wisconsin Space Science and Engineering Center's data center.

On this day, a strong short-wave trough was forecast to move into the upper Great Lakes, with ample instability (~2000–3000 J kg^{-1} of surface-based CAPE) ahead of a trailing surface cold front, creating an elevated hail and high-wind threat from southern Michigan to northeastern Oklahoma and northern Arkansas. Isolated storms began forming on and ahead of the front around 1700 UTC while the *GOES-14* SRSOR was in progress. Three storms are shown in this paper (Fig. 5): two from Arkansas and one from Missouri. Each storm had at least one severe-hail or severe-wind report associated with it. The maximum ε_{tot} and area of $\varepsilon_{tot} \geq 0.8$ are shown as functions of time after initial identification t_0 in Fig. 6. The gray dotted lines in each panel of Fig. 6 denote the endpoints of the 15-min interval of the *fastest* vertical (Figs. 6a,c,e) or horizontal (Figs. 6b,d,f) growth for each of the three storms. The 11-μm BT at the beginning and end of the interval of fastest vertical growth is also shown (Figs. 6a,c,e). The 1-min data yielded maximum $\Delta\varepsilon_{tot}$ from 0.06 to 0.1 min^{-1}. The Global Forecast System–estimated tropopause heights ranged from 14 000 to 14 200 m in the region during the rates of maximum vertical growth. The $\Delta\varepsilon_{tot}$ of these magnitudes in this range of tropopause heights yields maximum vertical velocities ~19–24 m s^{-1} (average over 1 min), which is similar to instantaneous maximum vertical velocities of deep convection found in recent observational studies (Heymsfield et al. 2010; Cecil et al. 2010). The 15-min-interval endpoints of each growth metric were used to create CDFs of the vertical and horizontal growth for each storm over that time period (Fig. 7) to compare with the 1-min-resolution time series over that time. The 15-min period of fastest growth illustrates a "best-case scenario" that current GOES routine operation scan mode would be able to capture (i.e., it is not dependent on where in the interval the scan would begin). For the vertical growth of storm 1 (Fig. 7a), 33% of its growth occurred in the first 8 min of the interval and the next 51% of its growth during this period occurred in the next 4 min (26.7% of the 15-min period). For the vertical growth of storm 3 (Fig. 7e), nearly 70% of the growth occurred in the first 6 min of the interval, in 40% of the 15 min. Storm 2 (Fig. 7c) grew vertically by 13% in the first minute (in 6.7% of the 15-min period), and the remainder of its vertical growth was mostly linear. This demonstrates that much of the vertical growth, especially the maximum growth rate in these storms, is not adequately resolved by 15-min temporal resolution. Five-minute temporal resolution would be needed to reasonably resolve vertical growth rates such as those exhibited by storms 1 and 3.

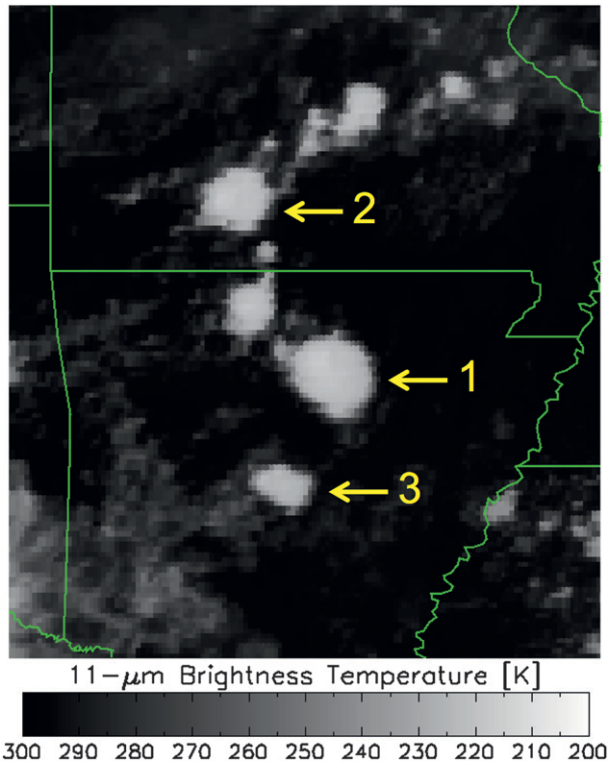

FIG. 5. The 11-μm BT from 1800 UTC 16 Aug 2012 over southern Missouri and Arkansas. The yellow numbers depict storms that are used for the time-series comparison (see Fig. 6, below). An animation of the storms' evolution from the visible channel and other SRSOR scenes is available online (http://cimss.ssec.wisc.edu/goes/srsor/GOES-14_SRSOR.html).

For the horizontal growth rates of these storms (Figs. 7b,d,e), most of the growth is fairly linear over the 15-min time intervals. Small spurts of growth do occur, but 10- or 15-min temporal resolution may be acceptable to capture the horizontal growth rates. Even so, the promise of consistent 5-min scans from GOES-R (Schmit et al. 2005) should help to alleviate the underresolution of vertical growth rates (which may hinder storm discrimination)

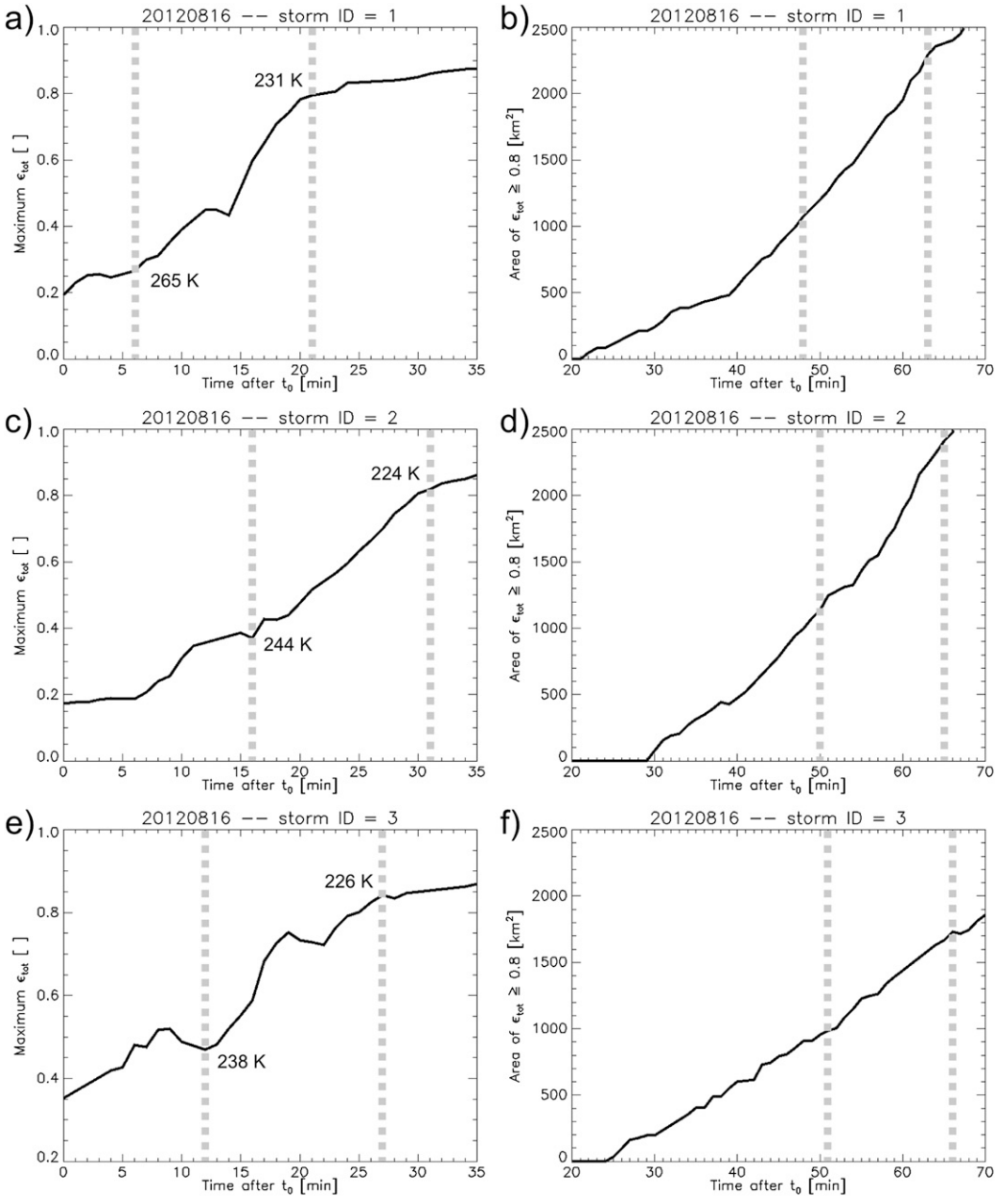

FIG. 6. Time series of (a),(c),(e) maximum ε_{tot} and (b),(d),(f) area of $\varepsilon_{tot} \geq 0.8$ as a function of minutes elapsed after initial time for (top to bottom) three severe thunderstorms on 16 Aug 2012. The storms grew during a period of 1-min *GOES-14* scans. The gray dotted lines represent the endpoints of the 15-min interval of fastest growth (vertically or horizontally). The annotations in (a),(c),(e) are the 11-μm BTs at the beginning and end of the intervals demarked by the dotted lines.

and to sharpen the accuracy of horizontal growth rates of thunderstorms.

4. Conclusions and future work

Robust satellite-derived cloud products were used to investigate growth rates of convective clouds prior to their maturation. Research on the trends of storms from geostationary imagery is not new; the approach used in this paper is unique, however. Excellent discernment between severe and nonsevere thunderstorms was demonstrated in several growth metrics. Two vertical growth metrics ($\Delta\varepsilon_{tot}$ and Δice) and two horizontal growth metrics ($\Delta\varepsilon_{tot\_area}$ and $\Delta\tau_{area}$) were shown to have very good

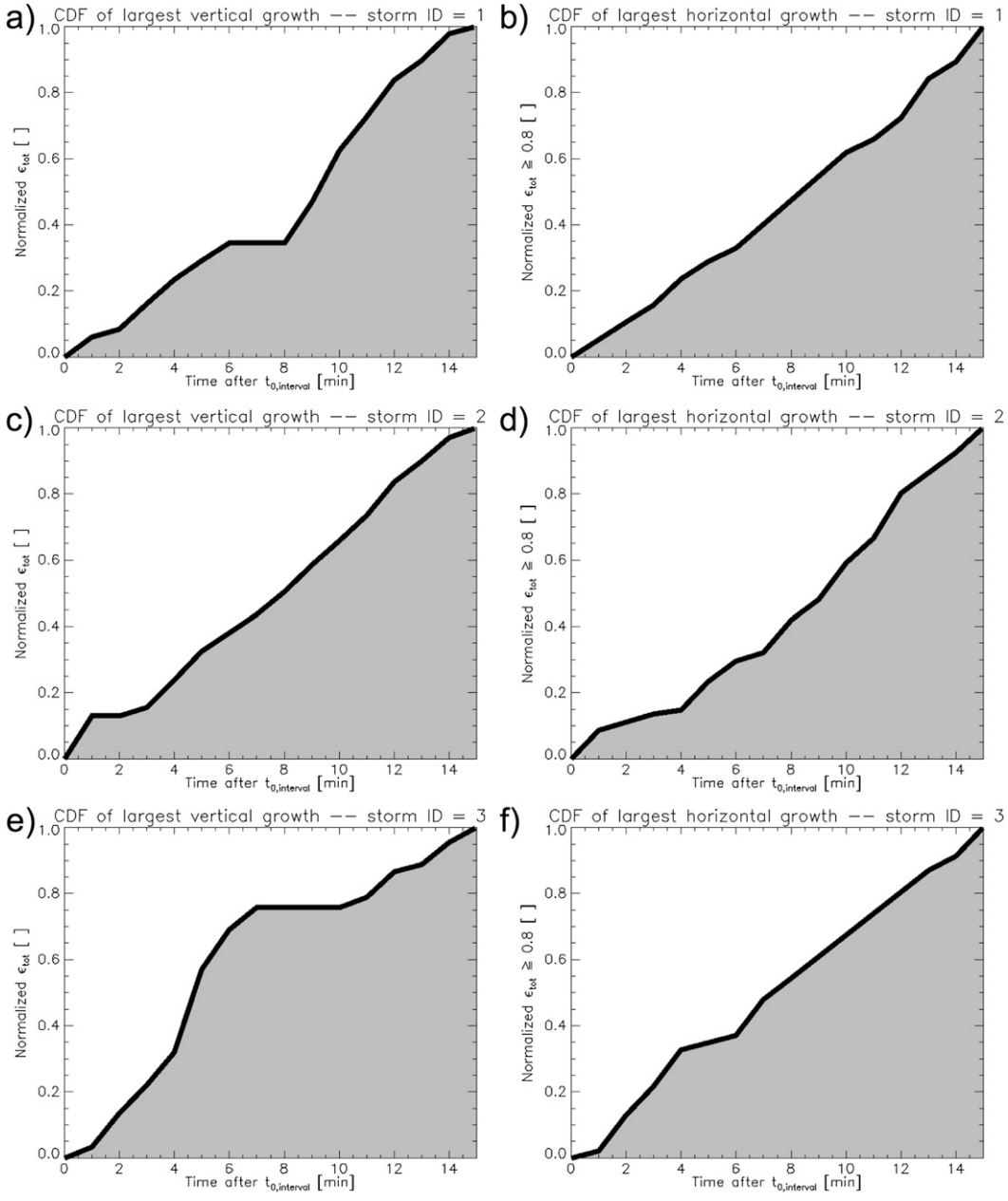

FIG. 7. CDFs of (a),(c),(e) maximum ε_{tot} and (b),(d),(f) area of $\varepsilon_{\text{tot}} \geq 0.8$ over the 15-min interval of fastest growth for each storm (depicted in Figs. 6a–f), as a function of elapsed minutes after initial time of the interval $t_{0,\text{interval}}$. The y axis is normalized by the 15-min period of growth.

classification value. Furthermore, $\Delta\varepsilon_{\text{tot}}$ and $\Delta\varepsilon_{\text{tot\_area}}$ demonstrated good lead time for a large proportion of storms for several radar predictors. All satellite-based predictors had appreciable lead time for low and moderate MESH and VIL values, whereas only the vertical predictor $\Delta\varepsilon_{\text{tot}}$ exhibited lead time on moderate REF10. The vertical predictors demonstrate more lead time than do the horizontal predictors for all radar thresholds. These results are consistent with Adler and Fenn (1979a), who related areal expansion of an isotherm and cloud-top cooling to the magnitude of updraft velocity and to severe-weather reports on the ground. Radar thresholds were selected to measure lead time in the study presented here, however. This research also demonstrated that satellite-observable storm properties evolve on small time scales (<5 min) and that current geostationary scan strategies are insufficient to completely capture the vertical and perhaps horizontal growth

rates of deep convection. Adler and Fenn (1979a) also suggested that short-interval (~5 min) scans are necessary to adequately sample storm growth rates. The maximum vertical velocities of strong thunderstorms derived from 1-min GOES imagery are comparable to the findings of recent observational studies of continental deep convection.

With excellent statistical and practical separation among the distributions of several GOES-derived growth metrics between severe and nonsevere thunderstorms, there is potential to better classify the future severity of developing convection and perhaps add lead time to radar-indicated warnings. A statistical model is currently being trained and evaluated with a combination of the satellite metrics discussed in this paper, numerical weather prediction output of storm environment, and radar metrics to predict the probability that a growing, unobscured convective cloud will produce severe weather at a later time. This fused method attempts to maximize the utility afforded by multiple sensors and platforms with high temporal and spatial resolutions on current observing systems. This and similar approaches hold promise not only in the present day but in the future as well, when sensors with improved coverage, resolution, and capabilities will have been deployed and integrated into the forecast process.

Acknowledgments. The authors acknowledge NOAA/GIMPAP for support of this research, as well as Valliappa Lakshmanan and Travis Smith at the University of Oklahoma/NOAA NSSL for providing radar data. Three anonymous reviewers also helped to improve the quality of this manuscript. The views, opinions, and findings contained in this report are those of the author(s) and should not be construed as an official National Oceanic and Atmospheric Administration or U.S. government position, policy, or decision.

REFERENCES

Adler, R. F., and D. D. Fenn, 1979a: Thunderstorm intensity as determined from satellite data. *J. Appl. Meteor.,* **18,** 502–517.

——, and ——, 1979b: Thunderstorm vertical velocities estimated from satellite data. *J. Atmos. Sci.,* **36,** 1747–1754.

——, M. J. Markus, and D. D. Fenn, 1985: Detection of severe Midwest thunderstorms using geosynchronous satellite data. *Mon. Wea. Rev.,* **113,** 769–781.

Cecil, D. J., K. R. Quinlan, and D. M. Mach, 2010: Intense convection observed by NASA ER-2 in Hurricane Emily (2005). *Mon. Wea. Rev.,* **138,** 765–780.

Cintineo, J. L., T. M. Smith, V. Lakshmanan, H. E. Brooks, and K. L. Ortega, 2012: An objective high-resolution hail climatology of the contiguous United States. *Wea. Forecasting,* **27,** 1235–1248.

Crum, T. D., and R. L. Alberty, 1993: The WSR-88D and the WSR-88D Operational Support Facility. *Bull. Amer. Meteor. Soc.,* **74,** 1669–1687.

Doswell, C. A., III, H. E. Brooks, and M. P. Kay, 2005: Climatological estimates of daily local nontornadic severe thunderstorm probability for the United States. *Wea. Forecasting,* **20,** 577–595.

Greene, D. R., and R. A. Clark, 1972: Vertically integrated liquid water—A new analysis tool. *Mon. Wea. Rev.,* **100,** 548–552.

Hansen, J. E., and L. D. Travis, 1974: Light scattering in planetary atmospheres. *Space Sci. Rev.,* **16,** 527–610.

Heidinger, A. K., 2010: Algorithm theoretical basis document: ABI cloud mask. NOAA/NESDIS/Center for Satellite Applications and Research Tech. Rep., 93 pp. [Available at http://www.goes-r.gov/products/ATBDs/baseline/Cloud_CldMask_v2.0_no_color.pdf.]

——, M. J. Pavolonis, R. E. Holz, B. A. Baum, and S. Berthier, 2010: Using *CALIPSO* to explore the sensitivity to cirrus height in the infrared observations from NPOESS/VIIRS and GOES-R/ABI. *J. Geophys. Res.,* **115,** D00H20, doi:10.1029/2009JD012152.

Heymsfield, G. M., and S. Schotz, 1985: Structure and evolution of a severe squall line over Oklahoma. *Mon. Wea. Rev.,* **113,** 1563–1589.

——, L. Tian, A. J. Heymsfield, L. Li, and S. Guimond, 2010: Characteristics of deep tropical and subtropical convection from nadir-viewing high-altitude airborne Doppler radar. *J. Atmos. Sci.,* **67,** 285–308.

Kain, J. S., and Coauthors, 2013: A feasibility study for probabilistic convection initiation forecasts based on explicit numerical guidance. *Bull. Amer. Meteor. Soc.,* **94,** 1213–1225.

Kelly, D. L., J. T. Schaefer, and C. A. Doswell III, 1985: Climatology of nontornadic severe thunderstorm events in the United States. *Mon. Wea. Rev.,* **113,** 1997–2014.

Lakshmanan, V., T. Smith, K. Hondl, G. J. Stumpf, and A. Witt, 2006: A real-time, three-dimensional, rapidly updating, heterogeneous radar merger technique for reflectivity, velocity, and derived products. *Wea. Forecasting,* **21,** 802–823.

——, A. Fritz, T. Smith, K. Hondl, and G. Stumpf, 2007a: An automated technique to quality control radar reflectivity data. *J. Appl. Meteor. Climatol.,* **46,** 288–305.

——, T. Smith, G. Stumpf, and K. Hondl, 2007b: The Warning Decision Support System-Integrated Information. *Wea. Forecasting,* **22,** 596–612.

Legeckis, R., 1975: Application of synchronous meteorological satellite data to the study of time dependent sea surface temperature changes along the boundary of the Gulf-Stream. *Geophys. Res. Lett.,* **2,** 435–438.

Lindsey, D. T., L. Grasso, 2008: An effective radius retrieval for thick ice clouds using GOES. *J. Appl. Meteor. Climatol.,* **47,** 1222–1231.

Mecikalski, J. R., and K. M. Bedka, 2006: Forecasting convective initiation by monitoring the evolution of moving cumulus in daytime GOES imagery. *Mon. Wea. Rev.,* **134,** 49–78.

——, P. D. Watts, and M. Koenig, 2011: Use of Meteosat Second Generation optimal cloud analysis fields for understanding physical attributes of growing cumulus clouds. *Atmos. Res.,* **102,** 175–190.

Menzel, W. P., and J. F. W. Purdom, 1994: Introducing GOES-I: The first of a new-generation of Geostationary Operational Environmental Satellites. *Bull. Amer. Meteor. Soc.,* **75,** 757–781.

Morgan, G. M., Jr., and P. W. Summers, 1982: Hailfall and hailstorm characteristics. *Thunderstorm Morphology and*

Dynamics, E. Kessler, Ed., 2nd ed., *Thunderstorms: A Social, Scientific and Technological Documentary,* Vol. 2, U.S. Government Printing Office, 363–408.

Mueller, C., T. Saxen, R. Roberts, J. Wilson, T. Betancourt, S. Dettling, N. Oien, and J. Yee, 2003: NCAR Auto-Nowcast System. *Wea. Forecasting,* **18,** 545–561.

Pavolonis, M. J., 2010a: Advances in extracting cloud composition information from spaceborne infrared radiances—A robust alternative to brightness temperatures. Part I: Theory. *J. Appl. Meteor. Climatol.,* **49,** 1992–2012.

——, 2010b: GOES-R Advanced Baseline Imager (ABI) algorithm theoretical basis document for cloud type and cloud base. NOAA/NESDIS/Center for Satellite Applications and Research Tech. Rep., 96 pp. [Available at http://www.goes-r.gov/products/ATBDs/baseline/Cloud_CldType_v2.0_no_color.pdf.]

Polger, P. D., B. S. Goldsmith, R. C. Przywarty, and J. R. Bocchieri, 1994: National Weather Service warning performance based on the WSR-88D. *Bull. Amer. Meteor. Soc.,* **75,** 203–214.

Purdom, J. F. W., 1993: Satellite observations of tornadic thunderstorms. *The Tornado: Its Structure, Dynamics, Prediction, and Hazards, Geophys. Monogr.,* Vol. 79, Amer. Geophys. Union, 265–274.

Reynolds, D. W., 1980: Observations of damaging hailstorms from geosynchronous satellite digital data. *Mon. Wea. Rev.,* **108,** 337–348.

Roberts, R. D., and S. Rutledge, 2003: Nowcasting storm initiation and growth using *GOES-8* and WSR-88D data. *Wea. Forecasting,* **18,** 562–584.

Rosenfeld, D., W. L. Woodley, A. Lerner, G. Kelman, and D. T. Lindsey, 2008: Satellite detection of severe convective storms by their retrieved vertical profiles of cloud particle effective radius and thermodynamic phase. *J. Geophys. Res.,* **113,** D04208, doi:10.1029/2007JD008600.

Schmit, T. J., M. M. Gunshor, W. P. Menzel, J. J. Gurka, J. Li, and A. S. Bachmeier, 2005: Introducing the next-generation Advanced Baseline Imager on GOES-R. *Bull. Amer. Meteor. Soc.,* **86,** 1079–1096.

Sieglaff, J. M., L. M. Cronce, W. F. Feltz, K. M. Bedka, M. J. Pavolonis, and A. K. Heidinger, 2011: Nowcasting convective storm initiation using satellite-based box-averaged cloud-top cooling and cloud-type trends. *J. Appl. Meteor. Climatol.,* **50,** 110–126.

——, D. C. Hartung, W. F. Feltz, L. M. Cronce, and V. Lakshmanan, 2013: A satellite-based convective cloud object tracking and multipurpose data fusion tool with application to developing convection. *J. Atmos. Oceanic Technol.,* **30,** 510–525.

Soden, B. J., 2004: The impact of tropical convection and cirrus on upper tropospheric humidity: A Lagrangian analysis of satellite measurements. *Geophys. Res. Lett.,* **31,** L20104, doi:10.1029/2004GL020980.

Suomi, V. E., and R. J. Parent, 1968: A color view of planet Earth. *Bull. Amer. Meteor. Soc.,* **49,** 74–75.

Trapp, R. J., D. M. Wheatley, N. T. Atkins, R. W. Przybylinski, and R. Wolf, 2006: Buyer beware: Some words of caution on the use of severe wind reports in postevent assessment and research. *Wea. Forecasting,* **21,** 408–415.

Vila, D. A., L. A. T. Machado, H. Laurent, and I. Velasco, 2008: Forecast and Tracking the Evolution of Cloud Clusters (ForTraCC) using satellite infrared imagery: Methodology and validation. *Wea. Forecasting,* **23,** 233–245.

Walther, A., and A. K. Heidinger, 2012: Implementation of the Daytime Cloud Optical and Microphysical Properties Algorithm (DCOMP) in PATMOS-x. *J. Appl. Meteor. Climatol.,* **51,** 1371–1390.

Wilks, D. S., 2006: *Statistical Methods in the Atmospheric Sciences.* 2nd ed. Elsevier, 627 pp.

Wilson, C. J., K. L. Ortega, and V. Lakshmanan, 2009: Evaluating multi-radar, multi-sensor hail diagnosis with high resolution hail reports. Preprints, *25th Conf. on Interactive Information Processing Systems,* Phoenix, AZ, Amer. Meteor. Soc., P2.9. [Available online at https://ams.confex.com/ams/pdfpapers/146206.pdf.]

Witt, A., M. D. Eilts, G. J. Stumpf, J. T. Johnson, E. D. Mitchell, and K. W. Thomas, 1998a: An enhanced hail detection algorithm for the WSR-88D. *Wea. Forecasting,* **13,** 286–303.

——, ——, ——, E. D. Mitchell, J. T. Johnson, and K. W. Thomas, 1998b: Evaluating the performance of WSR-88D severe storm detection algorithms. *Wea. Forecasting,* **13,** 513–518.

Young, A. H., J. J. Bates, and J. A. Curry, 2012: Complementary use of passive and active remote sensing for detection of penetrating convection from *CloudSat, CALIPSO,* and *Aqua* MODIS. *J. Geophys. Res.,* **117,** D13205, doi:10.1029/2011JD016749.

Zinner, T., H. Mannstein, and A. Tafferner, 2008: Cb-TRAM: Tracking and monitoring severe convection from onset over rapid development to mature phase using multi-channel *Meteosat-8* SEVIRI data. *Meteor. Atmos. Phys.,* **101,** 191–210.